HAL
open science

Confocal Volumetric μXRF and Fluorescence Computed μ-Tomography Reveals Arsenic Three-Dimensional Distribution within Intact Pteris vittata Fronds

Antony van Der Ent, Martin D de Jonge, Kathryn Spiers, Dennis Brueckner, Emmanuelle Montargès-Pelletier, Guillaume Echevarria, Xiaoming Wang, Mei Lei, Rachel Mak, James Lovett, et al.

To cite this version:

Antony van Der Ent, Martin D de Jonge, Kathryn Spiers, Dennis Brueckner, Emmanuelle Montargès-Pelletier, et al.. Confocal Volumetric μXRF and Fluorescence Computed μ-Tomography Reveals Arsenic Three-Dimensional Distribution within Intact Pteris vittata Fronds. Environmental Science and Technology, 2020, 54 (2), pp.745-757. 10.1021/acs.est.9b03878 . hal-02401572

HAL Id: hal-02401572

https://hal.science/hal-02401572v1

Submitted on 16 Nov 2020

HAL is a multi-disciplinary open access archive for the deposit and dissemination of scientific research documents, whether they are published or not. The documents may come from teaching and research institutions in France or abroad, or from public or private research centers.

L'archive ouverte pluridisciplinaire **HAL**, est destinée au dépôt et à la diffusion de documents scientifiques de niveau recherche, publiés ou non, émanant des établissements d'enseignement et de recherche français ou étrangers, des laboratoires publics ou privés.

Confocal volumetric µXRF and fluorescence computed µ-tomography reveals arsenic three-dimensional distribution within intact *Pteris vittata* fronds

Antony van der Ent[1,2*], Martin D. de Jonge[3], Kathryn M. Spiers[4], Dennis Brueckner[4,5,6], Emmanuelle Montargès-Pelletier[7], Guillaume Echevarria[2], Xiao-Ming Wan[8], Mei Lei[8], Rachel Mak[9], James Lovett[10], Hugh H. Harris[10*]

[1]Centre for Mined Land Rehabilitation, Sustainable Minerals Institute, The University of Queensland, Australia.

[2]Laboratoire Sols et Environnement, UMR 1120, Université de Lorraine, France.

[3]Australian Synchrotron, ANSTO, Australia.

[4]Photon Science, Deutsches Elektronen-Synchrotron DESY, Germany.

[5]Department of Physics, University of Hamburg, Germany.

[6]Faculty of Chemistry and Biochemistry, Ruhr-University Bochum, Germany.

[7]Laboratoire Interdisciplinaire des Environnements Continentaux, CNRS - Université de Lorraine, France.

[8]Center for Environmental Remediation, Institute of Geographic Sciences and Natural Resources Research, Chinese Academy of Sciences, China.

[9]Department of Chemistry, University of Sydney, Australia.

[10]Department of Chemistry, The University of Adelaide, Australia.

ABSTRACT

The fern *Pteris vittata* has been the subject of numerous studies because its extreme arsenic hyperaccumulation characteristics. However, information on the arsenic chemical speciation and distribution across cell types within intact frozen-hydrated *Pteris vittata* fronds is necessary to better understand the arsenic biotransformation pathways in this unusual fern. While 2D X-ray absorption spectroscopy imaging studies show that different chemical forms of arsenic – As(III) and As(V) – occur across the plant organs, depth-resolved information of arsenic distribution and chemical speciation in different cell types within tissues of *Pteris vittata* have not been reported. By using a combination of planar and confocal μ-X-ray fluorescence imaging and fluorescence computed μ-tomography, this study reveals the localization of Arsenic in the endodermis and pericycle surrounding the vascular bundles in the rachis and the pinnules of the fern. Arsenic is also accumulated in the vascular bundles connecting into each sporangium, and in some mature sori. The use of 2D X-ray absorption near edge structure imaging allows for deciphering arsenic speciation across the tissues, revealing arsenate in the vascular bundles and arsenite in the endodermis and pericycle. This study demonstrates how different advanced synchrotron X-ray microscopy techniques can be complementary in revealing, at tissue and cellular levels, elemental distribution and chemical speciation in hyperaccumulator plants.

Keywords: *chemical speciation; elemental distribution; hyperaccumulator; fern.*

1. INTRODUCTION

Hyperaccumulator plants are able to regulate potentially toxic concentrations of trace elements in their living tissues[1,2,3]. Arsenic hyperaccumulation has been described for a number of pteridophytes (ferns) from the genus *Pteris* (Pteridaceae), most notably *Pteris vittata*, which accumulates up to 22 600 μg g^{-1} As[4,5] and *Pityrogramma calomelanos* which accumulates up to 16 400 μg g^{-1} As[6,7] in fronds. Phytoextraction with *P. vittata* has been successfully applied in the remediation of soil and groundwater As[8,9,10]. The As hyperaccumulation mechanisms of *P. vittata* have elicited intensive research[11,12,13,14]. Arsenic content in *P. vittata* follows the order of pinnae > stipe > root, with most As distributed in the pinnae (78–96%). The concentration of As in the pinnae decreases from the base to the apex of the fronds, and As concentrations in midribs is much lower than in the pinnae[15]. The As concentration was relatively high in the midrib compared to the surrounding tissues, and there could be an unloading process of As from midrib to mesophyll tissues[16]. An interesting finding is that As concentrations in spores were far lower than in the pinnae, indicating that *P. vittata* tends to keep As away from reproductive organelles[15]. At the cellular level, energy dispersive X-ray spectroscopy combined to scanning electron microscopy (SEM-EDS) identified that As is primarily distributed within the upper and lower epidermis of the pinna in *P. vittata*[15]. Analysis with X-ray fluorescence imaging (μXRF) led to the reporting of even higher As concentration in trichomes compared that prevailing As concentrations in the epidermis[17]. At the subcellular level, As was mainly stored in the cytoplasmic supernatant fraction, accounting for 78% of As in the pinnae[18]. Therefore, As compartmentalisation in trichomes and vacuoles was suggested as a detoxification mechanism in *P. vittata*[15,17]. Recently, localization of As in the apoplast near the midrib, in fronds of *P. vittata* was reported[19]. A similarity between the As and K distribution at both cellular and subcellular level was found[15,20], implying that K^+ may act as a counterbalance to $As^VO_4^{3-}$ anions.

Pteris vittata contains As predominantly as inorganic As species[21]. Regardless of whether As(III) or As(V) was supplied to the plants, the oxidized form As(V) dominated in the roots while As(III) dominated in the rhizomes and fronds[15,21,22,23,24,25], suggesting that the reduction of As(V) to As(III) occurs during As translocation. Furthermore, X-ray absorption spectroscopy indicated that, in the pinnae, As(III) was predominantly coordinated with oxygen[22,25]. The precise location where As(V) is reduced to As(III) is still unknown. The reduction of As(V) to As(III) was firstly considered to occur in the pinnae as it was found that As in xylem sap was mainly As(V)[21,23]. It was proposed that As(V) is transported through the vascular tissue from the roots to the fronds, where it is reduced to As(III) and stored at high concentrations[25]. As(V) is reduced mainly in roots and not in the fronds[22,24] and root extracts from the *P. vittata* were able to reduce As(V) to As(III)[26]. The reduction of As mainly

occurs in the endodermis of roots[27]. Arsenic is transported in the xylem sap of *P. vittata* predominantly (93–98%) as As(III), regardless of whether As(V) or As(III) was supplied to the plants, implying that the roots are the main site of As(V) reduction in *P. vittata*[29]. Similar reduction of another metalloid, antimony (Sb), from pentavalent Sb to trivalent Sb has been reported in the roots of *P. vittata*[30]. However although clearly As(V) is reduced most effectively in root endodermis and then As(III) is transported most effectively in xylem, the identification of As(V) in other tissues means that not all of it is reduced in the root and the As(III) tris-glutathione [$As(SR)_3$] form found in the surroundings of the vasculature suggests that reduction can occur also outside the root[25].

Despite all the previously cited publications, no study to date has revealed the As-distribution at the cellular-scale in the *P. vittata* fronds, and previous data has only shown planar views of As (projected onto a 2D plane). As such no depth information is currently available and the *in situ* 3D distribution of As needs to be investigated and confirm the 2D visualisation. It is possible that observed differences in As speciation across tissues are due to spatial variations of As in different cell types[27,31]. Pickering *et al.*[25] examined both the gametophyte generation and the sporophyte generation, and found discrete speckles of arsenate localized in parenchymal cells (possibly in vacuoles) in the gametophytes. Another study on a related As-hyperaccumulating fern (*Pityrogramma calomelanos*) by Kachenko *et al.*[7] showed substantial tissue-level differentiation in As accumulation but could not reveal As chemical speciation.

Conventional synchrotron (planar or 2D) μXRF of plant leaves (whole leaves or cross sections) is a projection of all elements in a sample. As such, a planar view of a plant leaf reveals the elements contained in the adaxial and abaxial epidermis and mesophyll together in a 'compressed' projected 2D plane. Several methods are available for revealing the detailed 3D elemental distributions relevant to complex biological samples. In this article we employ three complementary approaches to access the 3D elemental distributions: mechanical sectioning to access the distributions within a single plane, X-ray fluorescence μ-computed tomography (XFM-μCT) to determine volumetric distributions from a series of projection images without sample sectioning, and confocal imaging to directly access elemental distributions within targeted regions within the specimen. Although we describe these methods here, a more detailed comparison can be found in de Jonge & Vogt[32] and van der Ent *et al.*[33].

Confocal optics enable a direct-space approach to deliver 3D resolution. A confocal optic confines the field of view of the energy-dispersive detector so that the signal derives from only a small portion

of the illuminated column[34,35,36]. The probe volume is thereby reduced to a spheroid and elemental distribution is mapped in three dimensions by scanning the specimen through the probe volume. The use of confocal X-ray fluorescence methods for the investigation of biological samples has been limited to date, probably due to the increased X-ray dose associated with the confocal geometry in most situations[37]. Such an approach was, however, successfully utilized to decipher the distribution and chemical speciation of selenium in zebrafish larvae[38].

Another approach to obtain information on the internal elemental distribution in physically intact samples is X-ray fluorescence μ-computed tomography (XFM-μCT). This technique enables reconstruction of 2D or 3D elemental data from a rotation series of projection images. For typical measurement modalities, μCT requires the measurement of projection images from multiples view around a fixed rotation axis. In order to avoid issues with self-absorption and to simplify the measurement, XFM-μCT is limited to measurements of specimen that are relatively thin in the two dimensions around the rotation axis, such as roots[39,40], stems and narrow leaves[41] and seeds[42], although μCT laminography could be used in flatter objects such as leaves. The confocal approach is more tolerant to self-absorption effects, and especially well-suited to measure depth profiles in extended planar objects such as leaves. Further, the confocal measurement enables direct access to small volumes within a specimen and so is amenable to direct and *in situ* spectroscopic (XANES) measurements.

Self-absorption is a combination of two effects that reduce the quantitative nature of reconstructions obtained by XFM-μCT and affect the visualization of element distribution: the absorption of the incident X-ray photons and the re-absorption of the fluorescent X-ray photons (in particular low-energy photons) by the specimen (for a review see Vogt & de Jonge[32]). Self-absorption is usually dominated by the latter of these effects, and this in turn has a greater impact on the quantitative determinations of the elements with low energy x-ray photons for K-shell emission this corresponds to with lower-*Z* elements. Self-absorption places a practical upper limit on the specimen dimensions, so that, for example, Ni can be mapped in hydrated biological samples up to ~800 μm thick with reasonable accuracy (Kα line at 7.47 keV), but this increases up to ~1500 μm for As (Kα line at 10.54 keV) assuming a tolerable limit of 50% self-absorption.

X-ray fluorescence microscopy (XFM) beamlines also offer the unique ability to perform *in situ* X-ray absorption spectroscopy (XAS) to obtain information on the chemical speciation of elements (As

in this case) in plant tissues without preparations and avoiding the possibility for artefacts resulting from those preparations. Moreover, the use of confocal optics allows examination of As chemical speciation at depth in distinct cell types within intact plant tissues and hence elucidation of the spatially resolved chemical speciation and elemental distribution in physically intact samples without the need for destructive sample preparation[33,43].

The complexity of As distribution and chemical speciation requires a range of different methodological approaches to understand the 3D distribution at the cellular level and also for the speciation. This study uses a combination of different synchrotron X-ray methodological approaches to interrogate As distribution and chemical speciation in *Pteris vittata* tissues, which are summarised in Table 1. To date, depth-resolved information has not been available, and this study aims not only to unravel the As pathway in the As hyperaccumulating fern *Pteris vittata*, but also to demonstrate how a set of advanced synchrotron X-ray microscopy techniques can be complementary in revealing, at tissue and cellular levels, the distribution and chemical speciation of As in this hyperaccumulator plant.

2. MATERIALS AND METHODS

2.1 Cultivation and collection of plant tissues and soils

Tissue samples were obtained in one of two ways. Cultured tissue samples were obtained from *P. vittata* grown in soil at the University of Queensland. The potting mix was spiked with an As(V) solution supplied as $Na_2HAsO_4 \cdot 7H_2O$ prior to transplanting (dose rate was 1000 mg kg^{-1} as As). The plants were grown in a greenhouse for two months with an 11-hr daily photoperiod, a photon flux of >370 μmol m^{-2} s^{-1}, a day-night temperature range of 20–29°C and relative humidity of ~70%. Tissue samples of *P. vittata* were also collected from a contaminated site in Shimen, Hunan Province in south China. This site is heavily contaminated by As due to realgar ore smelting activities in the past (N29°39’33.88” E111°2’43.1”) with a soil As concentration of 313 μg g^{-1}. The live plants, together with the soil attached to the roots, were transported from Hunan to Beijing, and maintained in the laboratory in Beijing. Tissue samples intended for synchrotron XFM analysis were excised with a razor blade and immediately shock-frozen using the metal mirror freezing technique (n which the sample is rapidly pressed against a block of solid copper cooled by at -196°C liquid N_2. The samples were then wrapped in Al-foil and transported in a cryogenic container (at least -190°C) for storage and transport. Samples were also freeze-dried in a freeze-dryer (LABCONCO FreeZone 6) starting at -50°C until room temperature in 48 hours. Slow freeze-drying has been shown to avoid, or at least,

187 reduce elemental re-distribution and tissue shrinkage[44,45] but may cause subcellular migration of
188 dissolved elements to the nearest solid surface. The influence of freeze-drying on element chemical
189 speciation is still contentious and depends on several factors such as the element itself, its chemical
190 speciation and initial oxidation state[46,47].
191
192 Some physical cross-sections were prepared from the cultivated *P. vittata* fronds. After shock
193 freezing (as described earlier), the samples were cryo-transferred on dry ice (-80°C) into the cryo-
194 chamber of the microtome (maintained at -30°C) and mounted on a plate by application of chilled (-
195 8°C) polypropylene glycol for physical support. The fronds were then cut to 30 µm sections using a
196 cooled blade (-20 °C), and the sections transferred to pre-cooled 1 mL cryo-containers and freeze-
197 dried.
198
199 **2.2 Plant tissue bulk analysis**
200 Plant tissue samples for bulk chemical analysis were gathered from the cultured ferns after two
201 months, and from the freeze-dried fern samples from China. The samples were dried at 70°C for five
202 days in a dehydrating oven, subsequently ground and a 200-mg fraction digested using 4 mL
203 concentrated nitric acid (70%) and 1 mL hydrogen peroxide (30%) in a digestion microwave oven
204 (Milestone Start D) for a 45-minute programme. After cooling, the sample was diluted to 30 mL with
205 TDI water. The aliquots were analysed on ICP-AES (Varian Vista Pro II) for P, Mg, Ca, K, S and
206 As.
207
208 **2.3 Histochemistry and bright field microscopy**
209 Frond samples were fixed in 3% glutaraldehyde (in PBS), sectioned with a vibratome (Leica
210 VT1000s) and stained with Toluidine Blue. The sections (20–40 µm thickness) were then examined
211 and photographed with bright field microscope (Nikon Diskovery Spinning Disk Confocal with
212 Andor Zyla 4.2 camera).
213
214 **2.4 Scanning Electron Microscopy with X-ray microanalysis (SEM-EDS)**
215 Freeze-dried leaf samples were sputter-coated with carbon (25 nm) and mounted on stubs. The
216 samples were then imaged with Scanning Electron Microscopy (SEM) with X-ray microanalysis
217 (Energy dispersive X ray spectroscopy or EDS) on a JEOL JSM-6610 instrument. Images were
218 obtained for 100–1000 x magnifications at 5–15 kV with lower accelerator energies for imaging with
219 secondary electrons only and higher accelerator energies for imaging using backscattered electrons.
220

221 **2.5 X-ray fluorescence microscopy (XFM)**

222 The X-ray fluorescence microscopy (XFM) beamline of the Australian Synchrotron employs an in-
223 vacuum undulator to produce a brilliant X-ray beam of 4.1–20 keV with a focus down to 1000 nm. A
224 Si(111) monochromator and a pair of Kirkpatrick-Baez (KB) mirrors deliver a monochromatic
225 focused incident beam onto the specimen[48]. The P06 beamline of PETRA III (Deutsches Elektronen-
226 Synchrotron; DESY) is also equipped with Si(111) monochromator and KB mirrors[49] producing X-
227 ray beam of 5–23 keV with a focus down to 300 nm. Both beamlines are equipped with a Maia
228 detector consisting of a large detector array to maximize the detection of fluorescence signal. The
229 Maia detector allows for high overall count-rates and uses an annular detector geometry, where the
230 beam passes though the detector and strikes the sample at normal incidence[50,51]. This geometry
231 enables a large solid angle (1.2 steradian) to maximize detected signal and reducing the dose and
232 potential damage to a specimen[52]. Maia is designed for event-mode data acquisition, where each
233 detected X-ray event is recorded, tagged by detector number in the array, position in the scan and
234 other metadata[53]. This approach eliminates readout delays and enables short pixel times (typically
235 down to 0.1 ms) and large pixel counts to be achieved for high definition imaging (typically 10–100
236 M pixels). The confocal experiment used a custom-made polycapillary collimating optic (XOS, input
237 focal distance 2.5 mm, input field of view 10.0 μm, transmission efficiency optimized for 17.4 keV
238 radiation) fitted on a Vortex SDD detector (Hitachi Vortex EM-90, 80mm^2, minimum energy of 1.6
239 keV, energy resolution 120 eV, operated in 90-degree geometry). The experimental setup at the
240 XFM beamline the Australian Synchrotron, showing both the Maia detector and SDD detector with
241 confocal optic, is shown in Fig 1.

242

243 On the XFM beamline, the confocal μXRF and μXAS experiments used a polycapillary optic fitted
244 on the SDD detector allowing for a depth resolution (*dz*) of ~10 μm (energy and hence element-
245 dependant), while the beam spot size using the KB mirrors was ~2 μm. The resolution of the
246 polycapillary optic limits the *z*-resolution (along beam axis) of confocal tomography, while the beam
247 spot size limits the x-y-resolution. Accordingly, samples can be raster imaged with an effective probe
248 volume probe of volume of ~10 × 2 × 2 μm. The scan was carried out in the *x*-*z* plane which samples
249 the two smallest dimension of the pinnule - a virtual section – so that the *y*-axis is not probed, with a
250 1 second per pixel dwell time. The confocal μ-XRF images were recorded using a beam incident
251 energy of 15.8 keV

252

253 The fluorescence 2D XANES imaging at the XFM beamline was performed on a portion of a frozen-
254 hydrated pinnule, spanning the midvein and one margin containing sporangia. The fluorescence 2D

XANES imaging consisted of forming 'stacks' of μXRF images by scanning the sample area multiple times at successive incident energies. As such, the sample was raster-scanned over a 2.380 ×. 1.295 mm window with a 5 μm step size, resulting in a μ-XANES image stack of 477 ×. 260 pixels. The sample was scanned over the As K-edge (11 877 eV) at 112 energies from 11 800 to 12 100 eV using 2 eV steps across the pre-edge region (11 800 to 11 855 eV), 0.5 eV steps across the XANES region (11 855 to 11 900 eV) and 20 eV across the post-edge region (11 900 to 12 100 eV). The μ-XANES spectra were measured using the Maia detector array with a ~1.7 ms per pixel dwell time.

Arsenic 'hotspots' were identified from the confocal μXRF images as regions of interest for volumetric XANES point measurements. Of particular interest is the reduction of arsenate to arsenite as As species cross from the vascular system to the leaf tissues, so regions were selected in the (tissues listed in decreasing proximity to main vascular system) midvein, endodermis, mesophyll and epidermis as well as regions in the secondary veins (vein bundles and surrounding protective sheaths) and sporangia (reproductive parts of the fern). In order to obtain spatial coordination, first coarse confocal μXRF maps were made of the sample. Volumetric XANES point measurements were acquired using the confocal optic attached to a Vortex SDD detector (as described above) and measured across the As K-edge (11 877 eV) at 100 energies spanning the energy range 11 802 to 12 017 eV in 0.25 eV steps with 0.5s dwell.

Energy calibration at the XFM beamline was achieved using a sample of solid sodium arsenite diluted in boron nitride. The "white line" peak energy of this sample was assumed to be 11874.4 eV.

The 2D μXRF and single-slice μXRF tomography measurements carried out in the microprobe of P06 at DESY were performed with a beam size of 532 × 444 nm at an incident energy of 14 keV. Considering a minimum step size of 0.5 μm and comparing it to the size of the beam, the resolution of the resulting images can be treated as being equal to the step size. Samples consisted of a free-standing rachis and two pinnule margins, one mounted between Ultralene films for 2D measurements and the other mounted inside a Kapton capillary for tomography. All scans were conducted in continuous-scanning mode to minimize dead-time between the exposures with dwell times between 1 ms and 10 ms. In the case of single-slice tomography, the rotation stage was the slow scanning axis and the longer scans of the rachis were divided into eight interlaced sub-scans to account for possible vertical drift of the sample. All the samples were either freeze-dried (rachis) or dehydrated (pinnule margin) and so a cryo-stream was not employed.

289 **2.6 Sample preparation and measurement conditions**

290 All frozen-hydrated samples were scanned in using a cryo-stream, whereas the freeze-dried samples
291 were scanned at room temperature (20°C). Individual freeze-dried pinnules were glued to carbon
292 sticks with cyanoacrylate (Fig 1b,c), but larger samples (*i.e.* the intact 'fresh/live' frond) were
293 sandwiched between two sheets of Kapton thin film (4 μm) stretched over a Perspex frame (Fig 1d)
294 magnetically attached to the *x*-*y* motion stage at atmospheric temperature (~20°C). The samples were
295 scanned 'on-the-fly' with a 1–5 ms per pixel dwell at an incident energy of 15.8 keV. The frozen-
296 hydrated samples were transferred under the N_2 cryo-stream (-100°C) and were maintained at dry ice
297 temperature during transfer – as such they were kept under cryogenic conditions from collection
298 through to the completion of measurement.

299

300 **2.7 Data analysis**

301 The Maia X-ray fluorescence data were analysed using GeoPIXE[54,55], and images were generated
302 using the Dynamic Analysis method[56,57]. Unfortunately, due to a technical error associated with the
303 data writing to the cluster storage the raw data of a number of 2D μXRF elemental maps were
304 irretrievably lost. However, real-time (RT) processing data from GeoPIXE were locally retained, and
305 the corresponding pseudo-elemental maps are included in the Supplementary Information.

306

307 Self-absorption, which can lead to inaccuracy in the determination of elemental concentration by
308 XRM, especially in 'thicker' samples, depends on the composition of the material, on the thickness
309 of the sample, on the localisation of the element to be detected and on the element itself (energy of
310 its X-ray fluorescence lines), on the distance between sample and the detector, on the energy of the
311 incident beam. Assuming that fern tissue has a similar composition and density to that of cellulose
312 ($C_6H_{10}O_5$) with an average thickness of 300 μm (a pinnule blade is somewhat thinner at ~80 μm
313 whereas a rachis is thicker at ~500 μm) and a density of 1.0 g cm^{-3} then it is assumed that the As
314 fluorescence (K_{alpha} line et 10.5 KeV) maximum absorption on escape is ~10%.

315

316 Confocal XRF imaging data were analysed with MAPS. Because the (element-dependant)
317 transmission efficiency of the polycapillary optic is not known, and because of the different
318 geometric orientations of the sample (resulting in varying X-ray flux on the sample), the confocal
319 elemental maps were not quantified with respect to concentrations of particular elements. The
320 concentrations are hence plotted on a relative scale.

321

322 Analysis of the XFM-μCT data was achieved by alignment steps using consistency and cross-
323 correlation methods to correct for horizontal drift in the sinograms followed by a tomographic
324 reconstruction step. The high angular sampling of the rachis allowed reconstruction using a filtered
325 back-projection algorithm. However, the pinnule sinograms were recorded with lower angular
326 sampling and so were reconstructed with a maximum-likelihood expectation-maximization algorithm
327 based on the functions of the *scikit-image* image processing library.
328
329 Fluorescence-XANES mapping gave a 3D image stack of spatial dimensions (x, y) and an X-ray
330 incident energy-resolved dimension E. Initially, the XANES images were aligned using a well-
331 featured spectator element. Alternatively, one could consider each pixel (x, y) of the 477 × 260-pixel
332 image stack to be associated with a unique XANES spectrum. The energy variation in the
333 fluorescence spectra were identified using principal component analysis (PCA) allowing for up to six
334 principal components, with the calculations performed using the Multivariate ANalysis Tool for
335 Spectromicroscopy (MANTiS, Lerotic). Pixels possessing similar spectra were grouped together by
336 *k*-means clustering, identifying three distinct clusters associated with the leaf, vein and image
337 background (Figure 10). The cluster associated with the background of the image has been
338 subtracted from composite image in Figure 10.
339
340 **3. RESULTS.**
341
342 **3.1 Bulk chemistry and anatomical features**
343 Although *P. vittata* can reach up to 22 600 μg g^{-1} As dry weight in its fronds[4], the cultured plants
344 display 1354 μg g^{-1} and field collected plants from China have 8580 μg g^{-1} As on a dry weight basis
345 (Table 2). The concentration of Ca is relatively high in the pinnae with up to 10 300 μg g^{-1}, whereas
346 the K concentration is extremely high in both the pinnae and rachis ranging from 12 300 to 33 000
347 μg g^{-1}. The concentration of P is exceptionally high, especially in the samples from China with up to
348 62 700 μg g^{-1} in the pinnae and up to 67 000 μg g^{-1} in the rachis. Concentrations of Cu, Zn and Fe are
349 unremarkable. Toluidine blue stained *P. vittata* sections of the rachis (Fig. 2) show the typical
350 anatomy of a pteridophyte with the C-shaped elliptical vascular bundles surrounded by three-cell
351 thick pericycle and endodermis cells. The mesophyll is not differentiated into palisade and spongy
352 parenchyma, and mesophyll is absent from the mid-rib. Scanning Electron Microscopy (SEM)
353 images show details of the sporangium with sporophytes (Fig. 3). Each sorus contains clusters of
354 sporangia protected by the upper indusial flap ('false indusium') that is formed by the margins of the

355 pinnule. The abundant presence of fertile cells is evident with the sporangium showing individual
356 sori enclosed by large annulus cells.
357
358 **3.2 Planar elemental imaging, confocal 'virtual' and computed tomography slices**
359 The 2D projection μXRF elemental maps of the live frond (Fig. 4) show substantial enrichment of
360 As in the vascular bundles, particularly in the rachis, but also in the veins of the pinnule. There is a
361 depletion of As in the interveinal areas of the pinnule. The localisation of K is similar except that its
362 concentration in the rachis is higher than the mean As concentration in fronds. In contrast, Ca is
363 depleted in the rachis, but enriched in the veins of the pinnule particularly towards the terminal ends.
364 Calcium is also enriched in damaged (chloric) parts of the fronds, mainly along the margins. These
365 differences are more pronounced in the high-resolution scans of the pinnule apex (Fig. 5), with Ca
366 depleted in the veins but enriched along the pinnule margins. The distribution of As and K are again
367 similar although the distribution of K extends into the lamina. In the freeze-dried pinnule portion
368 towards the terminus (Suppl. Fig. S1 A, B), the distribution of As mirrors that of the frozen-hydrated
369 samples with substantial enrichment in the vascular bundles, especially in the central vein. In fertile
370 pinnules (Suppl. Fig. 1, C, D) strong accumulation of As in the sorus and sporangia is visible.
371 Further detail can be gleaned from scans of the sori (Suppl. Fig. 2). Apart from As enriched in the
372 indusium, the strongest accumulation occurs in the annulus of each sporangium. Some of the
373 individual spores are also rich in As (see top-right panel, Fig. 9), as are hairs in the sorus (for
374 example bottom right panel Fig. 9). Enrichment in the hairs that guard the sporangium at the margin
375 of the fronds has been noted previously[25].
376
377 Higher resolution 2D μXRF images (up to 0.5 μm) were collected of the (freeze-dried) pinna margin
378 containing the indusium covering the sporangia, which reveals that As is enriched predominantly in
379 the vascular bundles connecting to the sporangia, but little in the sori themselves (Suppl. Figs. 6, 7,
380 and 8). K is enriched along the indusium edge, and Zn highly localised in the mature sori.
381 Fluorescence computed μ-tomography slices and projections of an intact pinna (Fig. 8 and 9, 0.5 μm
382 pixels) similarly reveal As enrichment in the vascular structures, especially in nodes, but also in
383 some sori.
384
385 Elemental maps of As, Br, Ca and Rb obtained from confocal 'virtual' cross-sections of a pinnule are
386 shown in Suppl. Fig. 9. The self-absorption effect as a function of element *z* is clearly visible from
387 the Ca elemental map with a 'shadow' evident behind the thicker midrib. For that reason, we have
388 plotted maps of (high *Z*) Rb and Br to serve as proxies for K and Cl respectively. The elemental

distribution of Rb is similar to As, which was expected on the basis of the earlier observed similarities between As and K. Arsenic is localised in the adaxial (upper) epidermis extending into the palisade mesophyll. Arsenic is also strongly enriched in the phloem of the (sub)lateral veins. Confocal cross-sections of the central part of the pinnule with the midrib reveal that As is strongly accumulated in the endodermis and pericycle surrounding the phloem (Fig. 6). Arsenic is also strongly enriched in abaxial (lower) epidermal cells of the midrib (but not extending to the lamina). Detailed confocal scans of the pinnule margins show accumulation of As in the indusium as well as in the sporangia, particularly the annulus (Suppl. Fig 10).

The elemental distribution of As in freeze-dried physical cross-sections scanned in 2D (Suppl. Fig. 3–4) also shows strong enrichment in the endodermis and pericycle surrounding the vascular bundles, as well as in the hypodermis extending into the cortex, ostensibly in the apoplastic space between the cells. Again, As is accumulated in the indusium and in the annulus of the sporangia. A scan of a physically sectioned freeze-dried rachis (Suppl. Fig. 5) shows the accumulation of As in the endodermis and pericycle surrounding the phloem. Fluorescence computed μ-tomography with 0.5 μm pixel size was undertaken on a freeze-dried rachis (Fig. 7) and reveals a very similar As enrichment pattern in the endodermis and pericycle surrounding the vascular bundles.

3.3 XANES imaging and volumetric XANES spot analysis

2D XANES imaging was performed on a frozen-hydrated pinnule. In addition, volumetric XANES measurements were acquired from spatial regions of interest in pinnae in both freeze-dried samples recorded at room temperature (Suppl. Figs. 11 and 12) and frozen-hydrated state under a cryostream using a confocal optic.

The cluster spectra associated with the pinnule and vascular bundle areas respectively were compared to reference spectra of relevant As standards (figure 10C). On the basis of the energy position of the absorption maxima, and comparison to the spectrum of solid sodium arsenite recorded during the same beamtime run, cluster 1 and 2 spectra were assumed to correspond to As(III) (as arsenite) and As(V) (as arsenate), respectively. Both spectra are slightly broadened in comparison with reference spectra reproduced from previous study[25] that were recorded with higher energy resolution (0.2 instead of 0.5 eV). However, the spectrum extracted from cluster 2 in Fig 10, primarily representing the main vascular bundle zone, displays an even broader absorption edge, displaying a shoulder at lower energy consistent with the peak energy of the arsenite model

spectrum. This broadening is likely due to the presence of a mixture of As(III) and (V) species in the vascular bundles, where the relative abundance of each species is consistent across the cluster.

Volumetric XANES point measurements from a selection of different anatomical features returned spectra that were distinct from the model compound spectra. Absorption peak energies were aligned more closely to those of the As(III) standards, even in tissues where As(V) would be expected from previous work and from the 2D XANES imaging in this work (Figure 10). For instance, it is expected that the vascular bundles (regions G and H, Suppl Fig. 11) would exhibit As(V) prior to crossing the endodermis, however these bundles display reduced As(III) as stated from the peak energy. The peak height to background edge jump ratio in several of the volumetric XANES spectra is drastically attenuated relative to the model spectra. The results of the volumetric XANES analysis suggest that this approach delivers too high of a radiation dose to the sample to be reliable in determining the speciation of As in the specimen without drastic photoreduction, even in samples cooled under a liquid N_2 cryostream. In fact, point XANES spectra from freeze-dried tissues (Suppl Fig 12), which should be less susceptible to photoreduction due to the absence of water, show higher peak energies in some cases compared to those spectra from frozen tissue, strongly implicating photodamage in the unusual appearance of these spectra.

The XANES spectra collected using either 2D XANES imaging or confocal point XANES are compared below to model As compound spectra previously reported[25]. We note that the spectral resolution of the beamline used in this work is significantly poorer than that from the previous work; as such, any comparison should be interpreted with caution as the spectra from this study will be broadened significantly compared to the model compound spectra.

4. DISCUSSION

The use of confocal optics has made it possible to examine As in the depth profile of the tissues in physically intact samples with high aspect ratio, without the need for destructive sample preparation, and this approach has provided new information on the mechanisms underlying As hyperaccumulation in *P. vittata.* Confocal cross-sections of the central part of the pinnule with the midrib have revealed that As is strongly accumulated in the endodermis and pericycle surrounding the phloem. XFM μ-CT revealed a very similar As enrichment pattern in the endodermis and pericycle surrounding the vascular bundles. As such, the various technical approaches lead to conclusions that are entirely consistent with each other.

Confocal optics also offer the ability to perform volumetric XANES to obtain spatially resolved information on the chemical speciation within intact tissues. However, it eventuated that volumetric XANES causes substantial photodamage due to the very high radiation dose of this approach (60s total exposure per point), even if the sample is cryogenically cooled. Therefore, observations indicate that significant interpretation regarding As chemical form should not be drawn from the confocal volumetric XANES measurements, and reiterate the utility of 2D XANES imaging to provide chemical information with lower X-ray dose (0.0017s total exposure per pixel, or ~300 less than then confocal XANES measurements), albeit without the capacity to provide information in the third dimension in this case. The results of the 2D XANES imaging are congruent with previous knowledge of As speciation in *P. vittata*[25], which in part validates the novel confocal imaging in this work as it demonstrates that the sample preparation has not modified the distribution of the primary arsenic species in the tissues. Published 2D XANES imaging studies showed that different chemical forms of As (As(III) and As-(V)) occur across the plant organs[25]. Depth information of As chemical speciation in different cell types within tissues of *P. vittata* was not available and the knowledge of the distribution across different cells types within the fronds and rachis was limited[28]. In this work we have demonstrated that observed differences in As speciation across tissues are related to spatial variation of As concentration in different cell types.

After the Zn-Ni-Cd hyperaccumulator *Noccaea caerulescens*, *P. vittata* is the most well-studied hyperaccumulator. As a consequence, much is now known about the uptake and metabolic regulation of As in this species[19,21,22,26,25,28,31,30]. Nevertheless, many open questions remain, specifically surrounding the adaptive advantages for As hyperaccumulation in this species, and about the physiological functions of As(V) to As(III) conversion for storage and translocation in the fronds.

Author contributions

M.L and X-M.W collected the *P. vittata* samples in the field in China. A.vdE cultivated live *P. vittata* in Australia. X-M.W prepared freeze-dried samples for the synchrotron analysis. A.vdE, M.dJ, E.M-P, G.E. and H.H.H conducted the synchrotron XFM experiments. M.dJ, R.MP and H.H.H analysed the XFM and XAS data. A.vdE performed the SEM-EDS and light microscopy experiments. A.vdE, K.M.S and D.B performed the synchrotron μXRF tomography experiments. K.M.S analysed the μXRF tomography spectra. D.B reconstructed the μXRF tomograms. All authors contributed to writing the manuscript.

Acknowledgements

This research was undertaken on the X-Ray Fluorescence Microscopy beamline of the Australian Synchrotron (part of ANSTO), Victoria, Australia. This work was supported by the Multi-modal Australian ScienceS Imaging and Visualisation Environment (MASSIVE). Beamtime at beamline P06 at PETRA III was granted within the in-house research program of DESY, a member of the Helmholtz-Association. We would like to thank Jan Garrevoet for assistance during the experiments. We thank the Centre for Microscopy and Microanalysis, The University of Queensland. A. van der Ent was the recipient of a Discovery Early Career Researcher Award (DE160100429) from the Australian Research Council. H. Harris acknowledges the Australian Research Council for financial support (DP140100176). The French National Research Agency through the national "Investissements d'avenir" program (ANR-10-LABX-21, LABEX RESSOURCES21) and through the ANR-14-CE04-0005 Project "Agromine" is acknowledged for funding support to A. van der Ent. Finally, the Program "Bingwei" Excellent Talent in the Institute of Geographic Sciences and Natural Resources Research, CAS supported this work.

REFERENCES

1 Krämer U. 2010. Metal Hyperaccumulation in Plants. Annu. Rev. Plant Biol. 61: 517–534.

2 Pollard AJ, Powell KD, Harper FA, Smith JAC. 2002. The Genetic Basis of Metal Hyperaccumulation in Plants. Critical Reviews in Plant Sciences 21: 539–566.

3 Reeves RD, Baker AJM, Jaffré T, Erskine PD, Echevarria G, van der Ent A. 2017. A global database for hyperaccumulator plants of metal and metalloid trace elements. *New Phytologist* 18: 407–411.

4 Ma LQ, Komar KM, Tu C, Zhang WH, Cai Y, Kennelley ED. 2001. A fern that hyperaccumulates arsenic. *Nature* 411(6836): 438-U3.

5 Tu C, Ma LQ. 2003. Effects of arsenate and phosphate on their accumulation by an arsenic-hyperaccumulator *Pteris vittata* L. Plant and Soil 249: 373–382.

6 Francesconi K, Visoottiviseth P, Sridokchan W, Goessler W. 2002. Arsenic species in an arsenic hyperaccumulating fern, *Pityrogramma calomelanos*: a potential phytoremediator of arsenic-contaminated soils. Science of the Total Environment, The 284: 27–35.

7 Kachenko AG, Bhatia NP, Singh B, Siegele R. 2007. Arsenic hyperaccumulation and localization in the pinnule and stipe tissues of the gold-dust fern (*Pityrogramma calomelanos* (L.) Link var. *austroamericana* (Domin) Farw.) using quantitative micro-PIXE spectroscopy. *Plant and Soil* 300: 207–219.

8 Chen, T., Li, H., Lei, M., Wu, B., Song, B., Zhang, X., 2010. Accumulation of N, P and K in *Pteris vittata* L. during phytoremediation: a five-year field study. Acta Sci. Circumstantiae 30, 402e408.

9 Xie Q-E, Yan X-L, Liao X-Y, Li X. 2009. The Arsenic Hyperaccumulator Fern *Pteris vittata* L. *Environmental Science & Technology* 43: 8488–8495.

10 Iriel, A., Lagorio, M.G., Cirelli, A.F., 2015. Biosorption of arsenic from groundwater using *Vallisneria gigantea* plants. Kinetics, equilibrium and photophysical considerations. Chemosphere 138, 383e389.

11 Vetterlein, D., Wesenberg, D., Nathan, P., Bräutigam, A., Schierhorn, A., Mattusch, J., Jahn, R., 2009. Pteris vittata Revisited: Uptake of As and ist speciation; impactof P, role of phytochelatins and S. Environ. Pollut. 157, 3016-3023

12 Poynton CY, Huang JW, Blaylock MJ, Kochian LV, Elless MP. 2004. Mechanisms of arsenic hyperaccumulation in *Pteris* species: root As influx and translocation. *Planta* 219: 1080–1088.

13 Danh LT, Truong P, Mammucari R, Foster N. 2013. A Critical Review of the Arsenic Uptake Mechanisms and Phytoremediation Potential of *Pteris vittata*. *International Journal of Phytoremediation* 16: 429–453.

14 Li JT, Gurilian K, Wu LH, van der Ent A, Qiu RL, Baker AJM, Tang YT, Yang X, Shu WS. 2018. Arsenic, cadmium, copper, manganese, REE, selenium and zinc hyperaccumulator plants from

China: a synthesis on the current state of knowledge. *Environmental Science & Technology* 52, 21: 11980-11994.

15 Lombi E, Zhao FJ, Fuhrmann M, Ma LQ. 2002. Arsenic distribution and speciation in the fronds of the hyperaccumulator *Pteris vittata*. *New Phytologist* 156: 195–203.

16 Chen TB, Huang ZC, Huang YY, Lei M. 2005. Distributions of arsenic and essential elements in pinnule of arsenic hyperaccumulator *Pteris vittata* L. *Science in China Series C-Life Sciences* 48(1): 18-24.

17 Li WX, Chen TB, Chen Y, Lei M. 2005. Role of trichome of *Pteris vittata* L. in arsenic hyperaccumulation. *Science in China Series C-Life Sciences* 48(2): 148–154.

18 Chen TB, Yan XL, Liao XY, Xiao XY, Huang ZC, Xie H, Zhai LM. 2005. Subcellular distribution and compartmentalization of arsenic in *Pteris vittata* L. *Chinese Science Bulletin* 50(24): 2843–2849.

19 Datta R, Das P, Tappero R, Punamiya P, Elzinga E, Sahi S, Feng H, Kiiskila J, Sarkar D. 2017. Evidence for exocellular Arsenic in Fronds of *Pteris vittata. Scientific Reports* 7: 579–8.

20 Huang ZC. Chen TB. Lei M. Liu YR. Hu TD. 2008. Difference of Toxicity and Accumulation of Methylated and Inorganic Arsenic in Arsenic-Hyperaccumulating and -Hypertolerant Plants. *Environmental Science & Technology* 42(14): 5106–5111.

21 Zhang, W. H.; Cai, Y.; Tu, C.; Ma, L. Q, 2002. Arsenic speciation and distribution in an arsenic hyperaccumulating plant. *Science of the Total Environment* 300(1-3): 167–177.

22 Huang ZC, Chen TB, Lei M, Hu TD. 2004. Direct determination of arsenic species in arsenic hyperaccumulator *Pteris vittata* by EXAFS. *Acta Botanica Sinica* 46(1): 46–50.

23 Kertulis GM, Ma, LQ, MacDonald GE, Chen R, Chen R, Winefordner JD, Cai Y. 2005. Arsenic speciation and transport in *Pteris vittata* L. and the effects on phosphorus in the xylem sap. *Environmental and Experimental Botany* 54 (3): 239–247.

24 Mathews S, Ma LQ, Rathinasabapathi B, Natarajan S, Saha UK. 2010. Arsenic transformation in the growth media and biomass of hyperaccumulator *Pteris vittata* L. *Bioresource Technology* 101(21): 8024–8030.

25 Pickering IJ, Gumaelius L, Harris HH, Prince RC, Hirsch G, Banks JA, Salt DE, George GN. 2006. Localizing the Biochemical Transformations of Arsenate in a Hyperaccumulating Fern. *Environmental Science & Technology* 40: 5010–5014.

26 Duan GL, Zhu YG, Tong YP, Cai C, Kneer R. 2005. Characterization of arsenate reductase in the extract of roots and fronds of Chinese brake fern, an arsenic hyperaccumulator. *Plant Physiology* 138(1): 461–469.

27 Lei M, Wan XM, Huang ZC, Chen, TB, Li, XW, Liu YR. 2012. First evidence on different transportation modes of arsenic and phosphorus in arsenic hyperaccumulator *Pteris vittata. Environmental Pollution* 161: 1–7.

28 Wan X, Lei M, Chen T, Ma J. 2017. Micro-distribution of arsenic species in tissues of hyperaccumulator *Pteris vittata* L. *Chemosphere* 166: 389–399.

29 Su YH, McGrath SP, Zhu YG, Zhao FJ. 2008. Highly efficient xylem transport of arsenite in the arsenic hyperaccumulator *Pteris vittata. New Phytologist* 180: 434–441.

30 Wan X, Lei M, Chen TB. 2016. Interaction of As and Sb in the hyperaccumulator *Pteris vittata* L.: changes in As and Sb speciation by XANES. *Environmental Science and Pollution Research*: 1–9.

31 Caille N, Zhao FJ, McGrath SP. 2004. Comparison of root absorption, translocation and tolerance of arsenic in the hyperaccumulator *Pteris vittata* and the nonhyperaccumulator *Pteris tremula*. New Phytologist 165: 755–761.

32 de Jonge MD, Vogt S. 2010. Hard X-ray fluorescence tomography-an emerging tool for structural visualization. *Current Opinion in Structural Biology* 20: 606–614.

33 van der Ent A, Przybyłowicz WJ, de Jonge MD, Harris HH, Ryan CG, Tylko G, Paterson DJ, Barnabas AD, Kopittke PM, Mesjasz-Przybyłowicz J. 2017. X-ray elemental mapping techniques for elucidating the ecophysiology of hyperaccumulator plants. *New Phytologist* 218: 432–452.

34 Kanngiesser B, Malzer W, Reiche I. 2003. A new 3D micro X-ray fluorescence setup — first archaeometric applications. *Nuclear Instruments and Methods in Physics Research Section B* 211: 259–264.

35 Janssens K, Proost K, Falkenberg G. 2004. Confocal microscopic X-ray fluorescence at the Hasylab microfocus beamline: characteristics and possibilities. *Spectrochimica Acta Part B* 59(533): 1637–1645.

36 Vincze L, Vekemans B, Brenker FE, Falkenberg G, Rickers K, Somogyi, Kersten SM, Adams F. 2004. Three dimensional trace element analysis by confocal X-ray microfluorescence imaging. *Analytical Chemistry* 76: 6786–6791.

37 Chukalina M, Simionovici A, Zaitsev S, Vanegas CJ. 2007. Quantitative comparison of X-ray fluorescence microtomography setups: Standard and confocal collimator apparatus. *Spectrochimica Acta Part B: Atomic Spectroscopy* 62: 544–548.

38 Choudhury S, Thomas JK, Sylvain NJ, Ponomarenko O, Gordon RA, Heald SM, Janz DM, Krone PH, Coulthard I, George GN, Pickering IJ. 2015. Selenium Preferentially Accumulates in the Eye Lens Following Embryonic Exposure: A Confocal X-ray Fluorescence Imaging Study. *Environmental Science & Technology* 49: 2255–2261.

39 Kopittke PM, Menzies NW, de Jonge MD, McKenna BA, Donner E, Webb RI, Paterson DJ, Howard DL, Ryan CG, Glover CJ, Scheckel KG, Lombi E. 2011. In Situ Distribution and Speciation of Toxic Copper, Nickel, and Zinc in Hydrated Roots of Cowpea. *Plant Physiology* 156: 663–673.

40 Lombi E, de Jonge MD, Donner E, Kopittke PM, Howard DL, Kirkham R, Ryan CG, Paterson D. 2011. Fast X-Ray Fluorescence Microtomography of Hydrated Biological Samples (JM Schnur, Ed.). *PLoS ONE* 6: e20626–5.

41 McNear DH Jr, Peltier E, Everhart J, Chaney RL, Sutton S, Newville M, Rivers M, Sparks DL. 2005. Application of quantitative fluorescence and absorption-edge computed microtomography to image metal compartmentalization in *Alyssum murale*. *Environmental Science & Technology* 39: 2210–2218.

42 Kim SA, Punshon T, Lanzirotti A, Li L, Alonso JM. 2006. Localization of iron in *Arabidopsis* seed requires the vacuolar membrane transporter VIT1. *Science* 314: 1295–1298.

43 Kopittke PM, Punshon T, Paterson DJ, Tappero RV, Wang P, Blamey FPC, van der Ent A, Lombi E. 2018. Synchrotron-Based X-Ray Fluorescence Microscopy as a Technique for Imaging of Elements in Plants. *Plant Physiology* 178: 507–523.

44 Tylko G, Mesjasz-Przybyłowicz J and Przybyłowicz WJ. 2007. X-ray microanalysis of biological material in the frozen-hydrated state by PIXE. *Microscopy Research and Technique* 70: 55–68.

45 Wang YD, Mesjasz-Przybylowicz J, Tylko G, Barnabas AD, Przybylowicz WJ. 2013. Micro-PIXE analyses of frozen-hydrated semi-thick biological sections *Nuclear Instruments and Methods in Physics Research Section B: Beam Interactions with Materials and Atoms* 306: 134–139.

46 George GN, Pickering IJ, Pushie MJ, Nienaber K, Hackett MJ, Ascone I, Hedman B, Hodgson KO, Aitken JB, Levina A, Glover C, Lay PA. 2012. X-ray-induced photo-chemistry and X-ray absorption spectroscopy of biological samples. *Journal of Synchrotron Radiation* 19: 875–886.

47 Wang P, McKenna BA, Menzies NW, Li C, Glover CJ, Zhao F-J, Kopittke PM. 2019. Minimizing experimental artefacts in synchrotron based X-ray analyses of Fe speciation in plant tissues of rice plants. *Journal of Synchrotron Radiation* 26. DOI: 10.1107/S1600577519004351

48 Paterson DJ, De Jonge MD, Howard DL, McKinlay WLJ, Starritt A, Kusel M, Ryan CG, Kirkham R, Moorhead G, Siddons DP. 2011. The x-ray fluorescence microscopy beamline at the Australian synchrotron. *AIP Conf. Proc*. 1365, 219.

49 Schroeder W, De Samber B. 2014. A Cryogenic Sample Environment for the Analysis of Frozen Hydrated Biological Tissue at the Hard X-ray Micro/Nano-Probe Beamline P06 at PETRA III. *Photon Science.*

50 Kirkham R, Dunn PA, Kucziewski A, Siddons DP, Dodanwela R, Moorhead GF, Ryan CG, De Geronimo G, Beuttenmuller R, Pinelli D, Pfeffer M, Davey P, Jensen M, Paterson D, de Jonge MD, Kusel M and McKinlay J, 2010, The Maia Spectroscopy Detector System: Engineering for Integrated Pulse Capture, Low-Latency Scanning and Real-Time Processing, *AIP Conference series* 1234: 240–243.

51 Siddons DP, Kirkham R, Ryan CG, De Geronimo G, Dragone A, Kuczewski AJ, Li ZY, Carini GA, Pinelli D, Beuttenmuller R, Elliott D, Pfeffer M, Tyson TA, Moorhead GF, Dunn *PA* 2014. Maia X-ray Microprobe Detector Array System. *Journal of Physics: Conference Serie*s 499: 012001–10.

52 Ryan CG, Kirkham R, Hough RM, Moorhead G, Siddons DP, de Jonge MD, Paterson DJ, De Geronimo G, Howard DL, Cleverley JS. 2010. Elemental X-ray imaging using the Maia detector array: The benefits and challenges of large solid-angle. *Nuclear Instruments and Methods in Physics Research Section A: Accelerators, Spectrometers, Detectors and Associated Equipment* 619: 37–43.

53 Ryan CG, Siddons DP, Kirkham R, Li ZY, de Jonge MD, Paterson DJ, Kuczewski A, Howard DL, Dunn PA, Falkenberg G, Boesenberg U, De Geronimo G, Fisher LA, Halfpenny A, Lintern MJ, Lombi E, Dyl KA, Jensen M, Moorhead GF, Cleverley JS, Hough RM, Godel B, Barnes SJ, James SA, Spiers KM, Alfeld M, Wellenreuther G, Vukmanovic Z, Borg S. 2014. Maia X-ray fluorescence imaging: Capturing detail in complex natural samples. *Journal of Physics: Conference Series* 499: 012002–12.

54 Ryan CG, Cousens DR, Sie SH, Griffin WL. 1990. Quantitative analysis of PIXE spectra in geoscience applications. *Nuclear Instruments and Methods in Physics Research Section B: Beam Interactions with Materials and Atoms* 49: 271–276.

55 C.G. Ryan, B.E. Etschmann, S. Vogt, J. Maser, C.L. Harland, E. van Achterbergh and D. Legnini, (2005), "Nuclear Microprobe – Synchrotron Synergy: Towards Integrated Quantitative Real-time Elemental Imaging using PIXE and SXRF", Nucl. Instr. Meth. B231, 183-188.

56 Ryan CG, Jamieson DN. 1993. Dynamic analysis: on-line quantitative PIXE microanalysis and its use in overlap-resolved elemental mapping. *Nuclear Instruments and Methods in Physics Research Section B: Beam Interactions with Materials and Atoms* 77: 203–214.

57 Ryan CG. 2000. Quantitative trace element imaging using PIXE and the nuclear microprobe. *International Journal of Imaging Systems and Technology* 11(4): 219–230.

FIGURE CAPTIONS

Figure 1. Experimental setup at the XFM beamline of the Australian Synchrotron: **[A]** Schematic diagram of confocal probe, SDD – silicon drift detector (image by Gary Ruben) **[B]** frozen-hydrated sample under the cryo-stream in front of the Maia detector; **[C]** Frozen-hydrated samples probed with the confocal optic; **[D]** Maia planar imaging at room temperature of a large live frond still attached to the plant (with rhizome in pouch with moist cotton). Typical dimensions of the probe beam are ~1 μm, those of the confocal field of view are ~10 um, and the specimen thickness is in the >100 μm domain.

Figure 2. Toluidine blue stained *Pteris vittata* sections: **[clockwise from top left]** section of the rachis; section of the central part of the frond; unstained and stained sections of the sporophytes attached to the frond. Abbreviations: *LE* lower epidermis, *UE* upper epidermis, *C* cortex, *P* pamenta, *VB* vascular bundle, *Ct* cuticle, *H* hypodermis, *M* mesophyll, *X* xylem, *E* endodermis, *Pe* pericycle, *Ph* phloem, *R* receptacle, *I* false indusium, *Ha* hair, *Ys* young sporangium, *Ms* mature sporangium, *A* annulus, *S* stomium.

Figure 3. Scanning Electron Microscopy (SEM) images of *Pteris vittata* tissues: **[A]** sporangium enclosures within the margin of the frond (indusium); **[B]** detail of sporophytes showing **[C]** vascular bundles of the rachis; **[D]** detail of central xylem bundles.

Figure 4. Planar μXRF maps of Ca, K and As of a live *Pteris vittata* frond examined at room temperature. Relative concentrations are depicted by shading with brighter colours equating to higher concentrations ('heatmap').

Figure 5. Planar μXRF maps of Ca, K, As and Compton Scatter of the terminal ends of a live *Pteris vittata* frond examined at room temperature. Relative concentrations are depicted by shading with brighter colours equating to higher concentrations ('heatmap').

Figure 6. Confocal μXRF virtual section elemental maps of As in *Pteris vittata* fronds (central part/rachis). Panels: **[A]** freeze-dried f examined at room temperature; **[B]** frozen-hydrated examined under the cryostream; **[C]** freeze-dried f examined at room temperature; **[D]** frozen-hydrated examined under the cryostream. Relative concentrations are depicted by shading with brighter colours equating to higher concentrations ('heatmap').

Figure 7 Single-slice µXRF tomogram of a freeze-dried *Pteris vittata* rachis examined at room temperature showing As and Compton signals. Relative concentrations are depicted by shading with brighter colours equating to higher concentrations ('heatmap').

Figure 8. Single-slice µXRF tomograms of a freeze-dried *Pteris vittata* pinnule margin inside a Kapton capillary examined at room temperature showing As and Compton signals. Relative concentrations are depicted by shading with brighter colours equating to higher concentrations ('heatmap').

Figure 9. 2D µXRF maps of a freeze-dried *Pteris vittata* pinnule margin inside a Kapton capillary examined at room temperature showing As and Compton signals from different angles. Relative concentrations are depicted by shading with brighter colours equating to higher concentrations ('heatmap').

Figure 10. *Left:* As elemental map of a portion of *Pteris vittata* pinnule including midvein and leaf margin, taken at the top energy of the 2D XANES imaging scan (12.1 keV). *Middle:* composite of cluster maps generated by *k*-means clustering analysis with $k = 3$. Cluster 1 is shown and blue and cluster 2 is shown in red, the third cluster associated with the image background has been set to white. *Right:* the spectra of cluster 1 and cluster 2 reconstructed from principal components compared to reference As standards. The sample is frozen-hydrated examined under the cryostream. Relative concentrations are depicted by shading with brighter colours equating to higher concentrations ('heatmap').

TABLE CAPTIONS

Table 1. Comparison of synchrotron X-ray methodological approaches that are available to an experimenter at XFM beamlines to interrogate As distribution and chemical speciation in Pteris vittata tissues. The exact values will change with the beamline.

Table 2. Bulk elemental concentrations in fronds of *Pteris vittata* (values as ranges and means in μg g^{-1} dry weight) with ICP-AES.

Supporting Information

Planar µXRF maps of As distribution in dehydrated *Pteris vittata* pinnule (Figure S1). Planar µXRF maps of As distribution in dehydrated *Pteris vittata* pinnule (Figure S2). Planar µXRF maps of As and K of a dehydrated cross-sectioned *Pteris vittata* pinnule (central portion) (Figure S3). Planar µXRF maps of As and K of a dehydrated cross-sectioned *Pteris vittata* pinnule (Figure S4). Planar µXRF maps of As and K of a dehydrated cross-sectioned *Pteris vittata* rachis (Figure S5). Planar µXRF maps of the K, As, Zn and Compton signals of a dehydrated *Pteris vittata* pinnule margin (Figure S6). Planar µXRF maps of the K, As, Zn and Compton signals of a dehydrated *Pteris vittata* pinnule margin (Figure S7). Planar µXRF maps of the K, As, Zn and Compton signals of a dehydrated *Pteris vittata* pinnule margin (Figure S8). Confocal µXRF maps of As, Br, Ca and Rb in a freeze-dried *Pteris vittata* pinnule showing the varying degrees of self-absorption depending on element *z* (Figure S9). Confocal µXRF maps of As in *Pteris vittata* pinnule (terminal end/sporangium) (Figure S10). As fluorescence map from confocal µXRF imaging of *P. vittata* sporangia recorded using the Vortex SDD from an incident beam energy of 15.8 keV, showing the locations of the volumetric XANES measurements taken at the sporangia, As fluorescence map from confocal µXRF imaging of *P. vittata* midvein, volumetric XANES spectra taken from the ROIs identified (Figure S11). Supplementary Figure 12. As fluorescence map from confocal µXRF imaging of *P. vittata* sporangia, volumetric XANES spectra taken from the ROIs identified (Figure S12). Bright-field microscopy images of transversely cut sections of *Pteris vittata* samples (Figure S13).

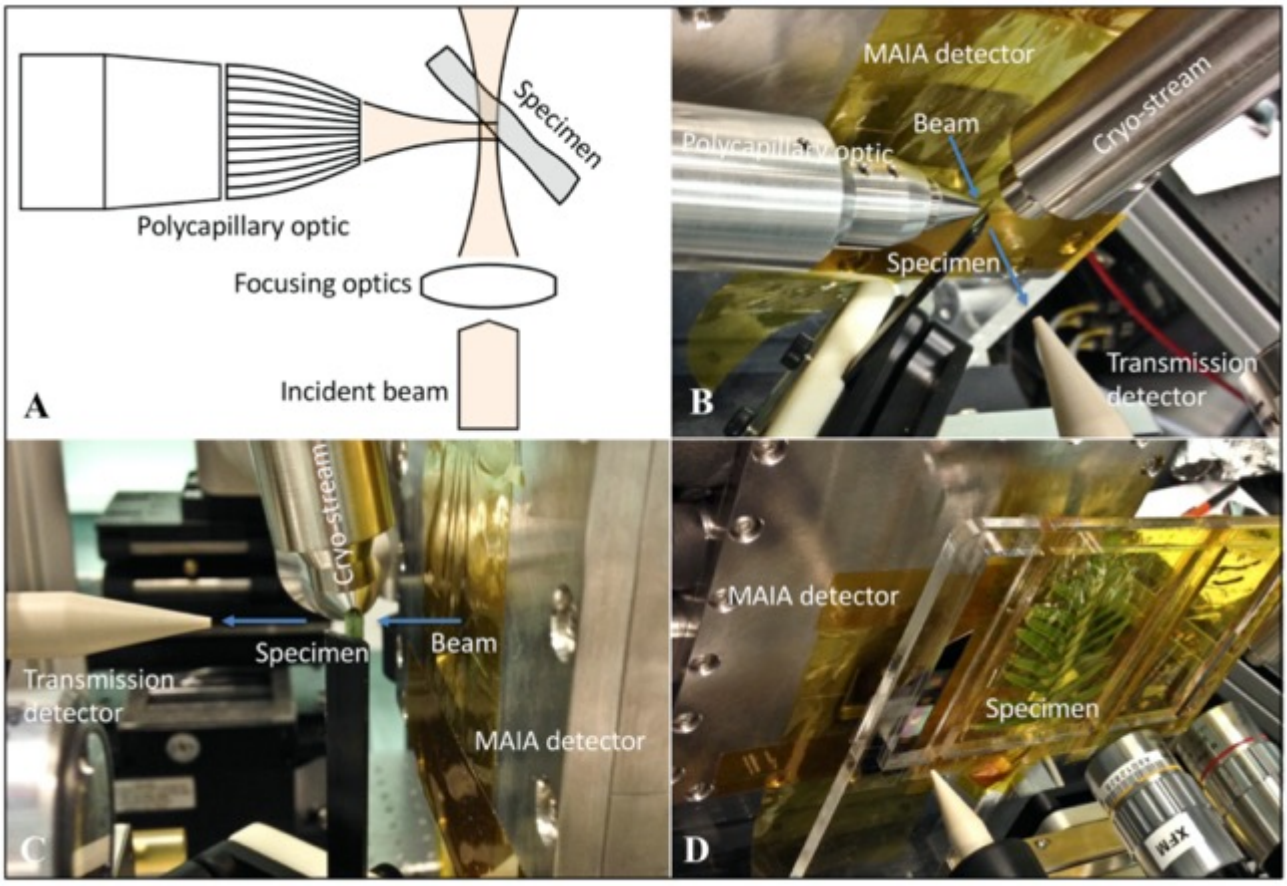

Figure 1. Experimental setup at the XFM beamline of the Australian Synchrotron: **[A]** Schematic diagram of confocal probe, SDD – silicon drift detector (prepared by Gary Ruben) **[B]** frozen-hydrated sample under the cryo-stream in front of the Maia detector; **[C]** Frozen-hydrated samples probed with the confocal optic; **[D]** Maia planar imaging at room temperature of a large live frond still attached to the plant (with rhizome in pouch with moist cotton). Typical dimensions of the probe beam are ~1 μm, those of the confocal field of view are ~10 um, and the specimen thickness is in the >100 μm domain.

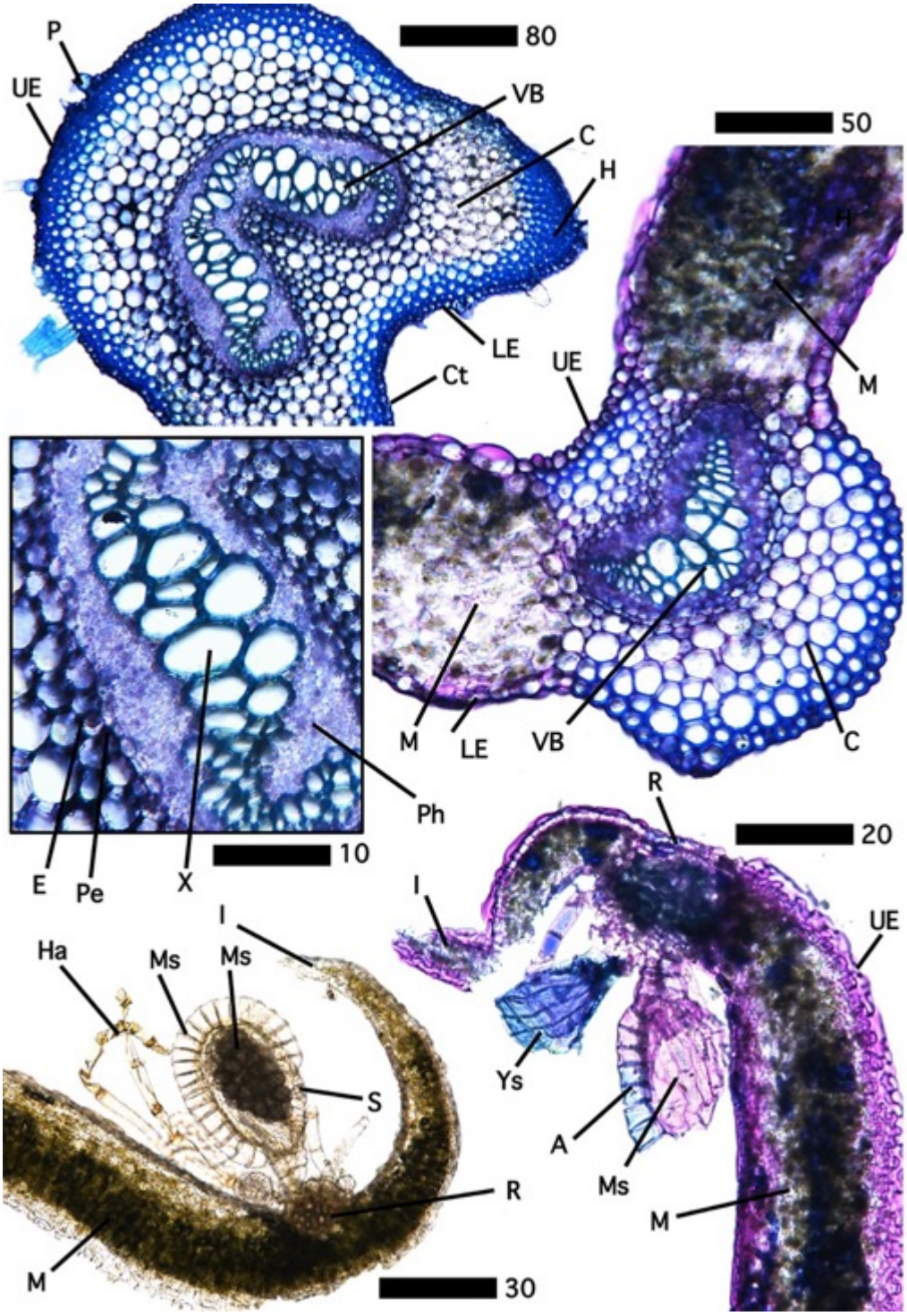

Figure 2. Toluidine blue stained *Pteris vittata* sections: **[clockwise from top left]** section of the rachis; section of the central part of the frond; unstained and stained sections of the sporophytes attached to the frond. Abbreviations: *LE* lower epidermis, *UE* upper epidermis, *C* cortex, *P* pamenta, *VB* vascular bundle, *Ct* cuticle, *H* hypodermis, *M* mesophyll, *X* xylem, *E* endodermis, *Pe* pericycle, *Ph* phloem, *R* receptacle, *I* false indusium, *Ha* hair, *Ys* young sporangium, *Ms* mature sporangium, *A* annulus, *S* stomium. Scale bars denote µm.

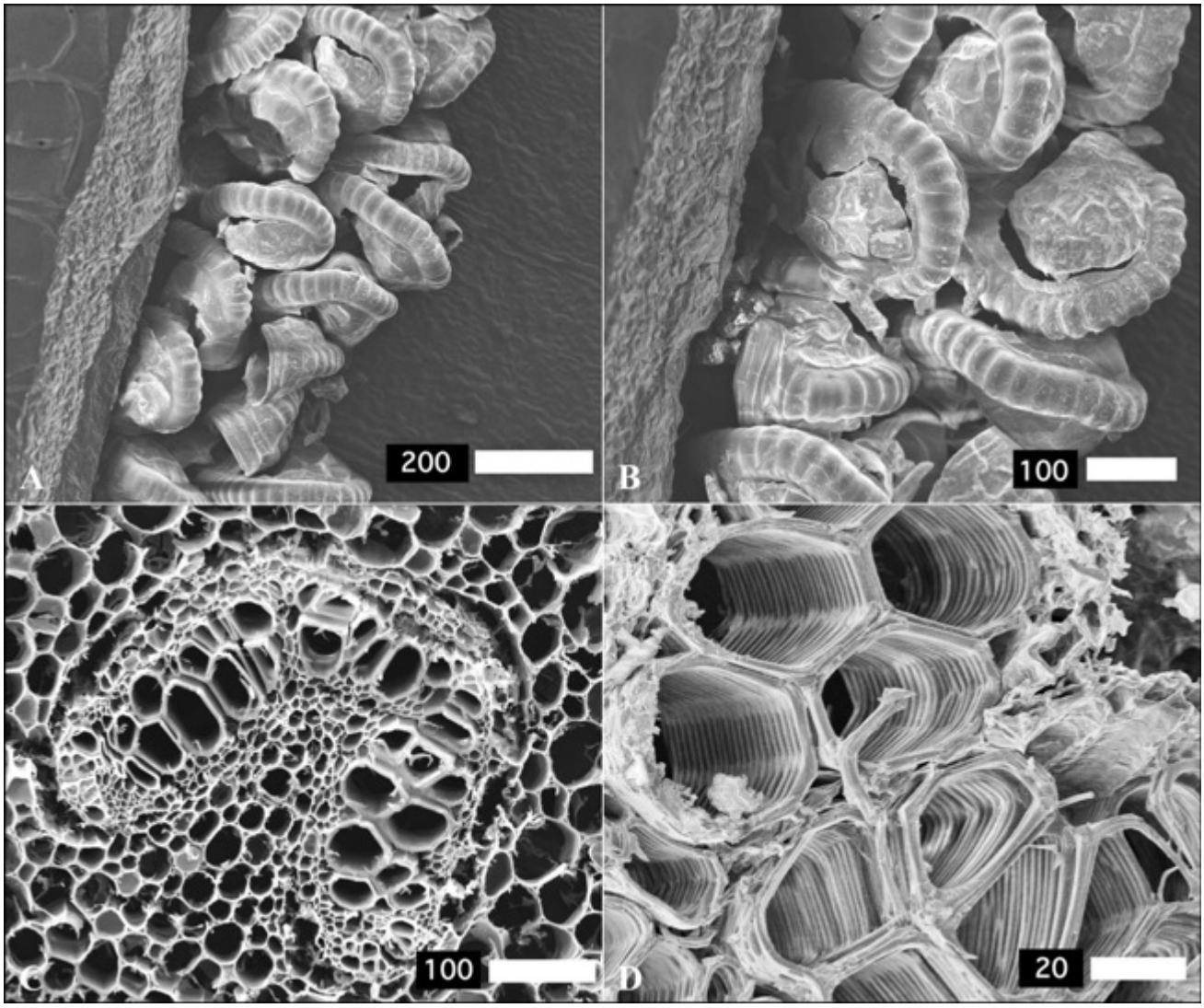

Figure 3. Scanning Electron Microscopy (SEM) images of *Pteris vittata* tissues: **[A]** sporangium enclosures within the margin of the frond (indusium); **[B]** detail of sporophytes showing **[C]** vascular bundles of the rachis; **[D]** detail of central xylem bundles. Scale bars denote µm.

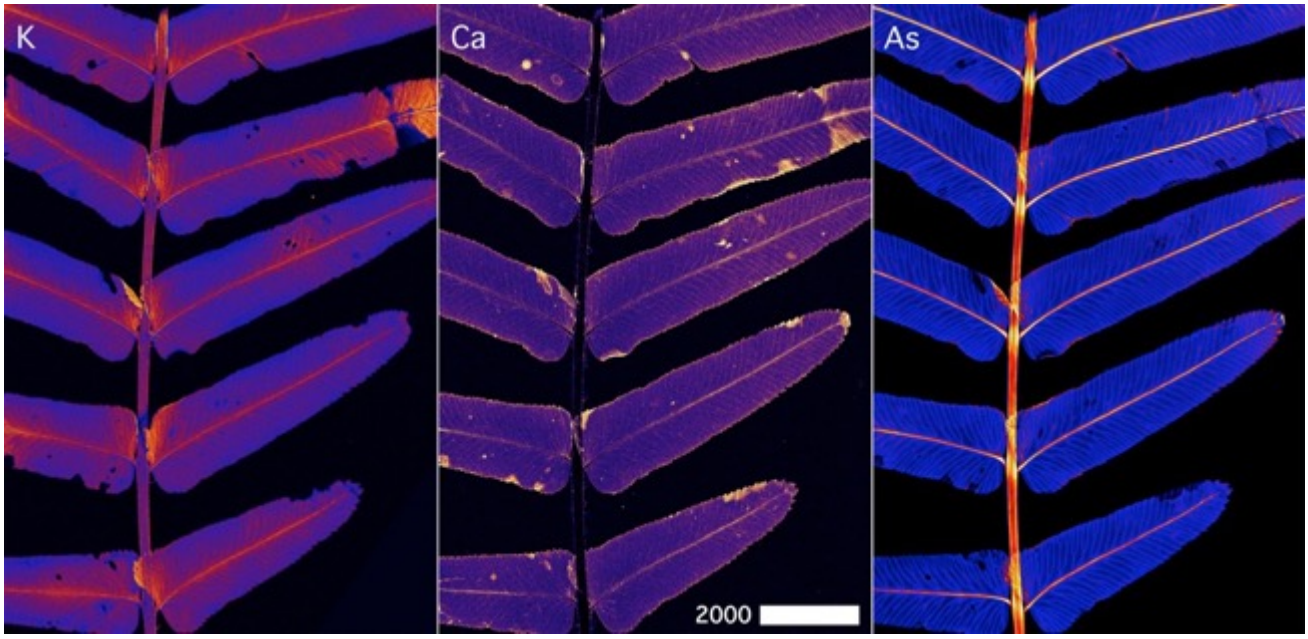

Figure 4. Planar µXRF maps of Ca, K and As of a live *Pteris vittata* of a partial frond with pinnae examined at room temperature. Relative concentrations are depicted by shading with brighter colours equating to higher concentrations ('heatmap'). Scale bars denote µm.

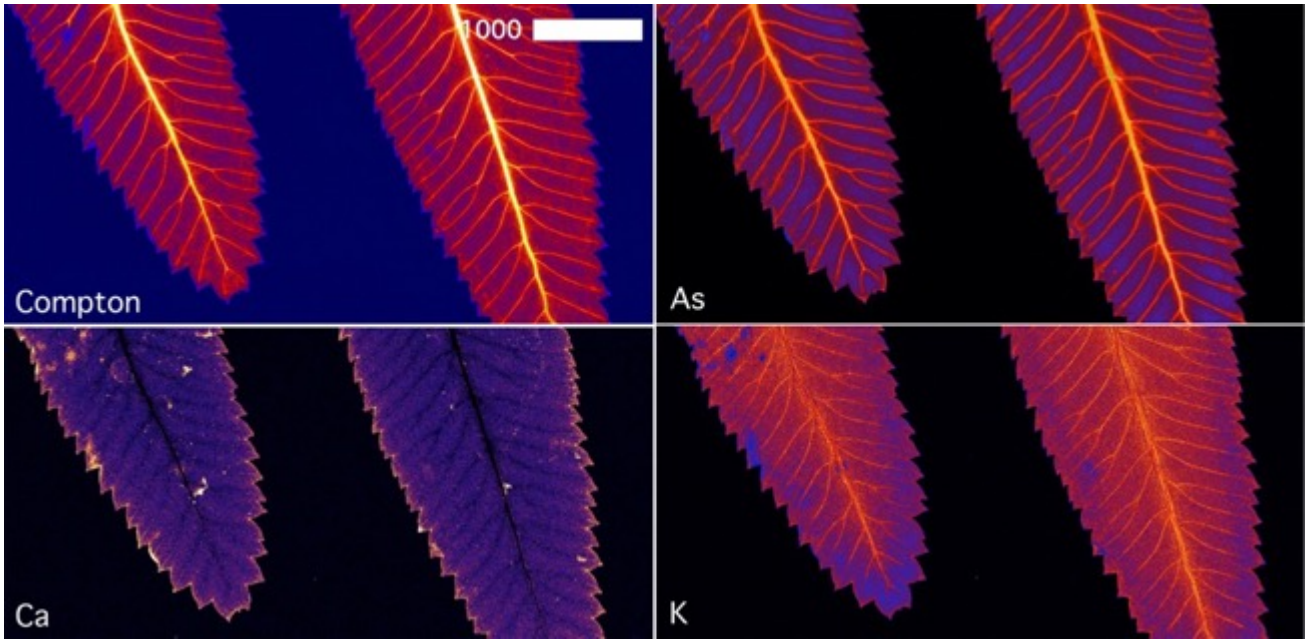

Figure 5. Planar µXRF maps of Ca, K, As and Compton Scatter of the terminal ends of a live *Pteris vittata* pinnules examined at room temperature. Relative concentrations are depicted by shading with brighter colours equating to higher concentrations ('heatmap'). Scale bars denote µm.

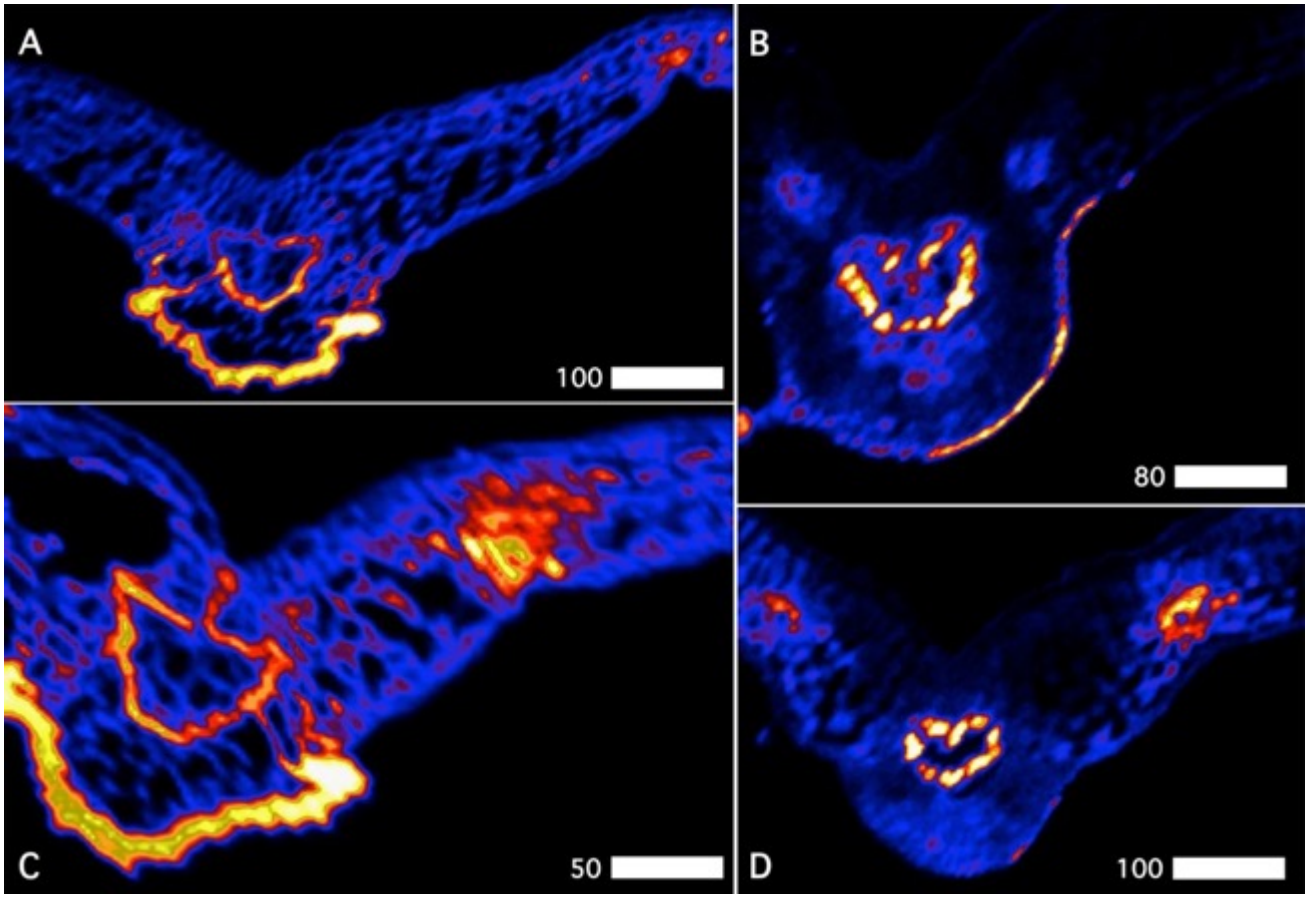

Figure 6. Confocal µXRF virtual section elemental maps of As in *Pteris vittata* pinnules (central part/rachis). Panels: **[A]** freeze-dried f examined at room temperature; **[B]** frozen-hydrated examined under the cryostream; **[C]** freeze-dried f examined at room temperature; **[D]** frozen-hydrated examined under the cryostream. Relative concentrations are depicted by shading with brighter colours equating to higher concentrations ('heatmap'). Scale bars denote µm.

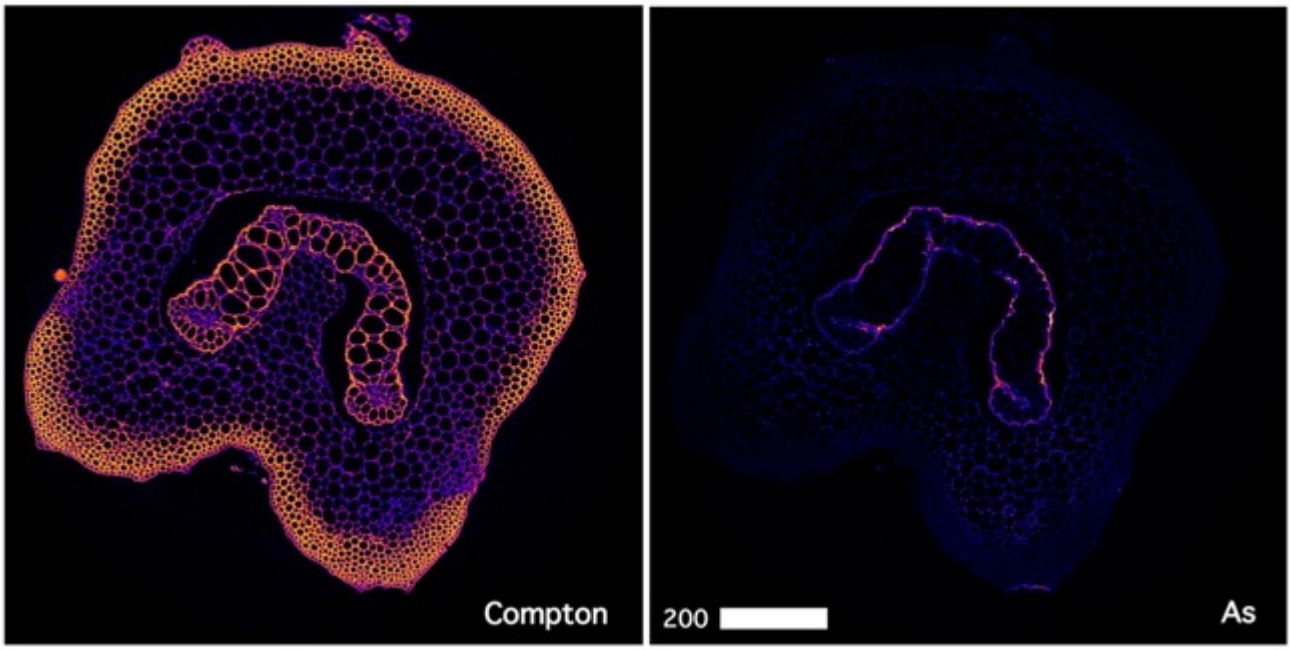

Figure 7 Single-slice µXRF tomogram of a freeze-dried *Pteris vittata* rachis examined at room temperature showing As and Compton signals. Relative concentrations are depicted by shading with brighter colours equating to higher concentrations ('heatmap'). Scale bars denote µm.

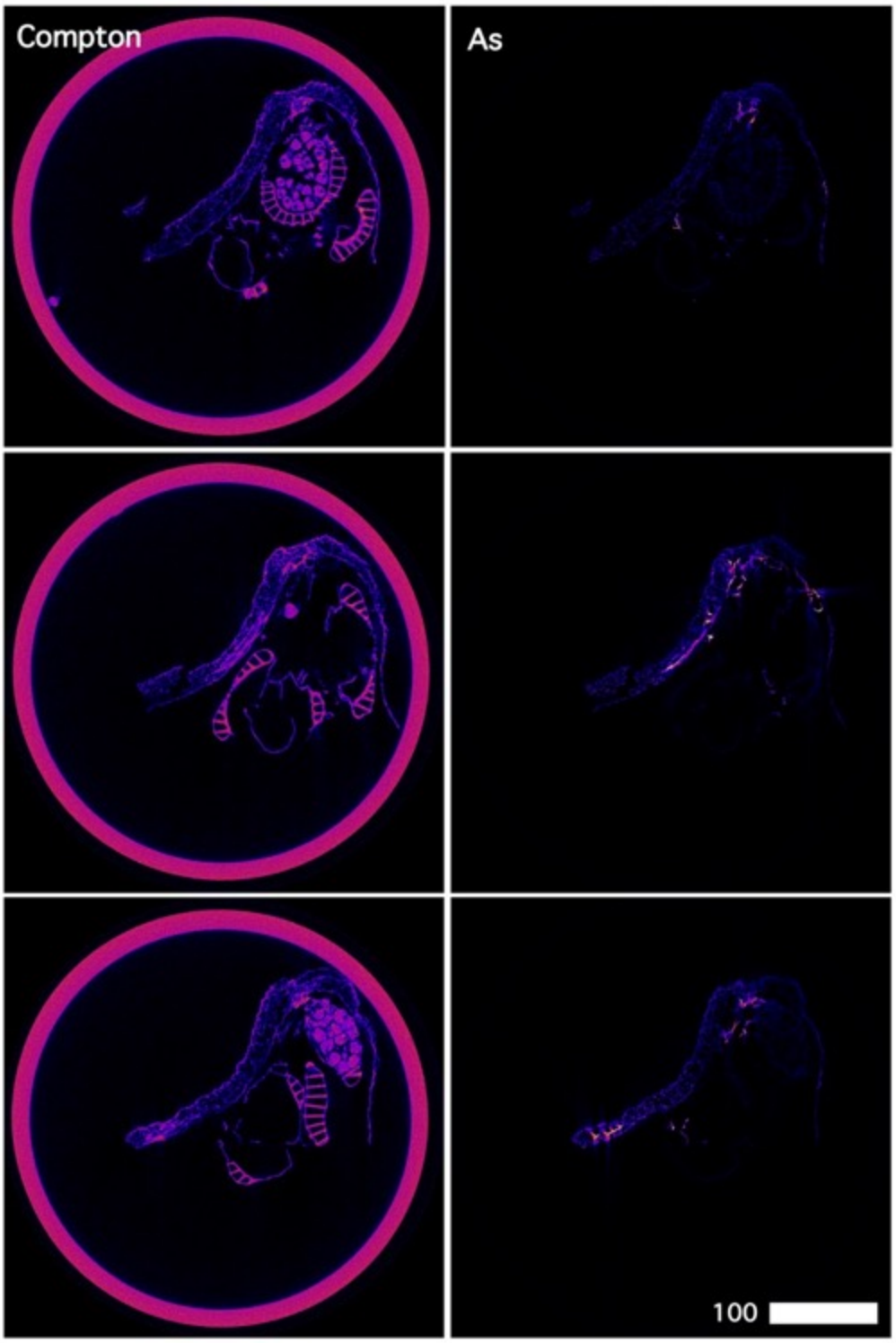

Figure 8. Single-slice µXRF tomograms of a freeze-dried *Pteris vittata* pinnule margin inside a Kapton capillary examined at room temperature showing As and Compton signals. The same sample at different depths is shown. Relative concentrations are depicted by shading with brighter colours equating to higher concentrations ('heatmap'). Scale bars denote µm.

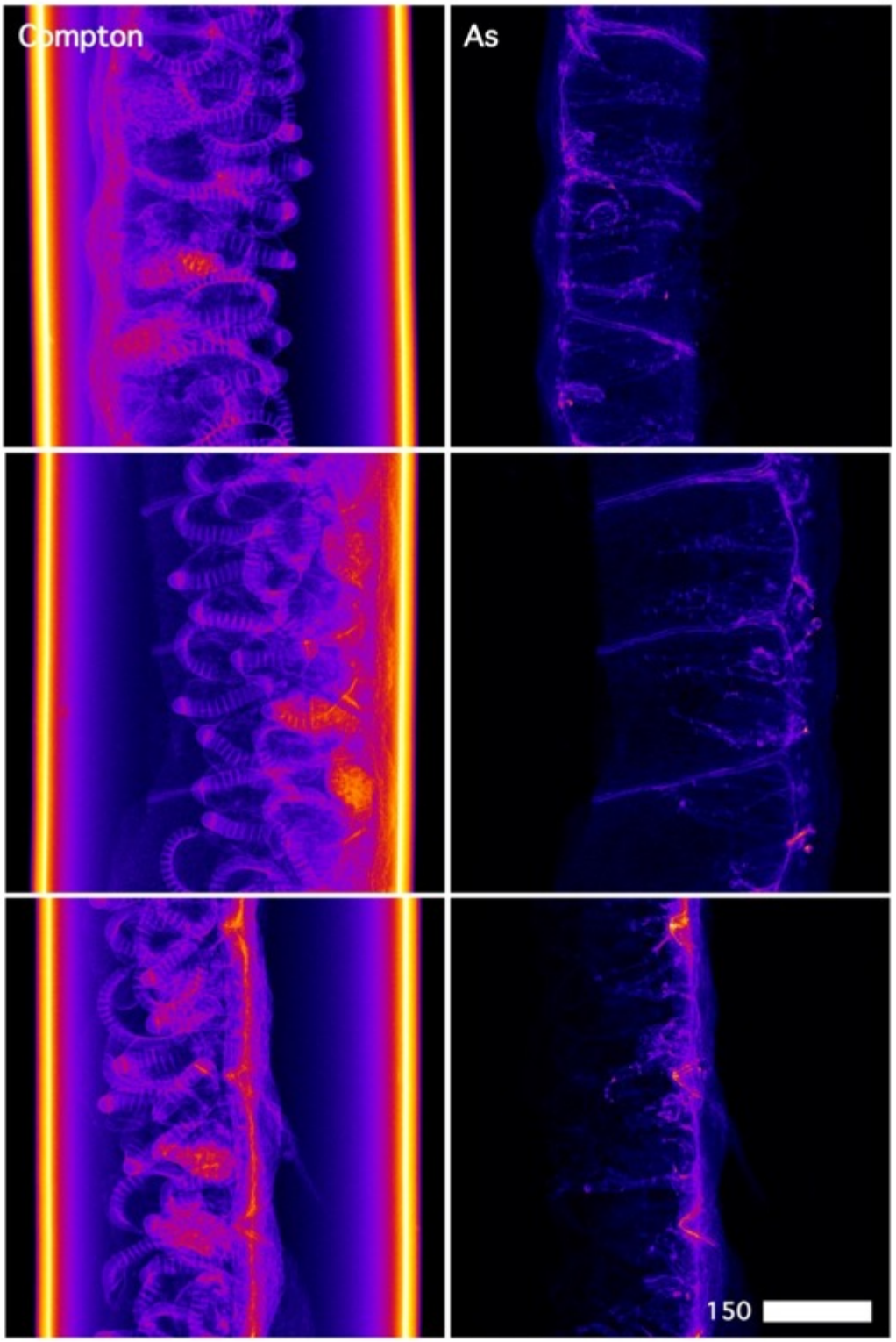

Figure 9. 2D µXRF maps of a freeze-dried *Pteris vittata* pinnule margin inside a Kapton capillary examined at room temperature showing As and Compton signals from different angles. Relative concentrations are depicted by shading with brighter colours equating to higher concentrations ('heatmap'). Scale bars denote µm.

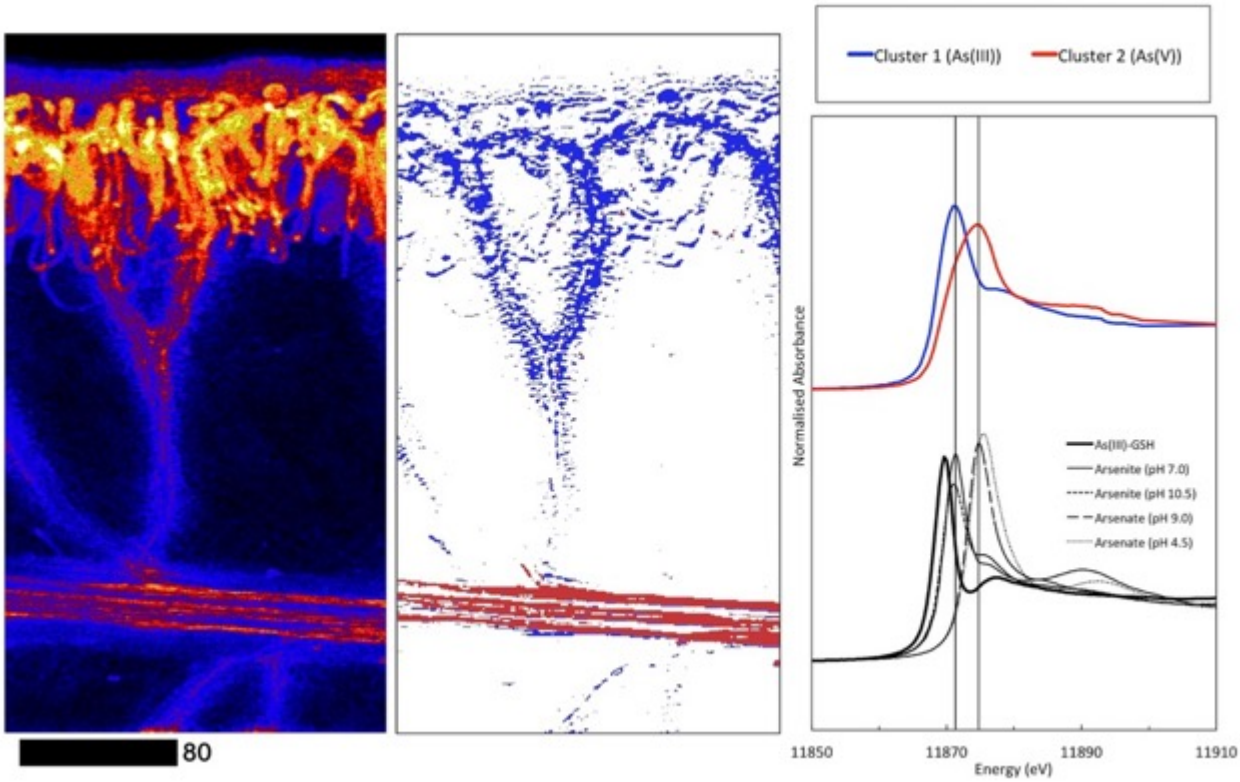

Figure 10. *Left:* As elemental map of a portion of *Pteris vittata* pinnule including midvein and leaf margin, taken at the top energy of the 2D XANES imaging scan (12.1 keV). *Middle:* composite of cluster maps generated by *k*-means clustering analysis with $k = 3$. Cluster 1 is shown and blue and cluster 2 is shown in red, the third cluster associated with the image background has been set to white. *Right:* the spectra of cluster 1 and cluster 2 reconstructed from principal components compared to reference As standards. As the energy calibration of the standards was not performed at the beamline, both cluster spectra have been shifted down in energy by 1 eV to align the peaks more closely with those of the standards. The sample is frozen-hydrated examined under the cryostream. Relative concentrations are depicted by shading with brighter colours equating to higher concentrations ('heatmap'). Scale bars denote µm.

Analysis Type	Specimen preparation	Specimen state	Imaging Modality	X, Y, (Z) resolution [µm]	Positive aspects	Negative aspects
µXRF	Sections	Dry or Frozen-hydrated	Projection imaging	2, 2, (30)	Fast acquisition Section thickness can match cellular length-scales	Disruptive preparation due to freeze-drying and/or sectioning
	Intact tissues	Frozen-hydrated	Projection imaging	2, 2, (none)	Fast acquisition Full specimen immobilisation	Narrow field of view depending on cryogenic implementation No depth information
	Intact tissues	Live hydrated	Projection imaging	0.5, 0.5, (none)	Fast acquisition Potential for sample evolution and degradation during analysis	Potential for radiation damage No depth information
	Intact tissues	Live hydrated / Dry	3D tomography	5, 5, 5	Ability to obtain 3D models of intact specimen	Potential for radiation damage Only for narrow specimen
	Intact tissues	Live hydrated / Dry	2D (single-slice) tomography	0.5, 0.5, 0.5	Acquisition of a single high-resolution virtual slice	Potential for radiation damage Only for narrow specimens
	Intact tissues	Frozen-hydrated	Confocal imaging	2, 2, 10	Direct access to internal volumes within extended specimens	Slower acquisition Increased radiation dose
XANES	--	--	XANES imaging	2, 2, (none)	Overall low radiation dose	No depth information
	--	--	Confocal XANES	2, 2, 10	Directly probes chemical speciation within internal volume	High radiation dose can result in photo-reduction

Table 1. Comparison of synchrotron X-ray methodological approaches that are available to an experimenter at XFM beamlines to interrogate As distribution and chemical speciation in *Pteris vittata* tissues. The exact values will change with the beamline.

Tissue	Origin	Sample preparation	As	Ca	Cu	Fe	K	Mg	Na	P	S	Zn
Pinnae	China	Freeze-dried	6130	4420	21	309	32 100	3650	3960	62 700	4410	93
Pinnae	China	Freeze-dried	8580	4620	29	281	33 000	4290	7190	55 000	4920	35
Pinnae	Cultured	Freeze-dried	777	6700	7.5	390	16 300	2620	1320	17 000	3070	28
Pinnae	Cultured	Freeze-dried	1130	10 300	8.3	203	12 300	3680	927	12 000	3100	40
Rachis	Cultured	Freeze-dried	1080	923	10	142	25 000	715	7702	37 600	1520	48
Rachis	Cultured	Freeze-dried	1350	924	10	171	24 300	682	7900	35 400	1440	34
Rachis	Cultured	Freeze-dried	1140	1620	8.2	145	27 300	1020	6570	34 200	2100	48
Rachis	China	Freeze-dried	4530	5760	16	313	24 900	4110	6740	67 000	3790	93
Whole frond	Cultured	Analysed living	5170	2180	15	152	33 000	2440	4440	27 300	2630	27

Table 2. Bulk elemental concentrations in fronds of *Pteris vittata* (values as ranges and means in μg g^{-1} dry weight) with ICP-AES.